Remote Sensing of Environment 311 (2024) 114314

Contents lists available at ScienceDirect

Remote Sensing of Environment

journal homepage: www.elsevier.com/locate/rse

Automating the detection of hydrological barriers and fragmentation in wetlands using deep learning and InSAR

Clara Hübinger [a,*], Etienne Fluet-Chouinard [b,c], Gustaf Hugelius [a], Francisco J. Peña [a,d], Fernando Jaramillo [a,e]

[a] Stockholm University, Department of Physical Geography, Sweden
[b] Earth System Science Division, Pacific Northwest National Laboratory, Richland, WA, USA
[c] Institute for Atmospheric and Climate Science, Department of Environmental Systems Science, ETH Zurich, Zürich, Switzerland
[d] Karolinska Institutet, Stockholm, Sweden
[e] Baltic Sea Centre, Stockholm University, Stockholm, Sweden

ARTICLE INFO

Edited by Menghua Wang

Keywords:
Wetlands
InSAR
Barriers
Connectivity
Deep learning
Segmentation

ABSTRACT

The loss of hydrological connectivity and fragmentation of natural wetlands are widespread drivers of wetland degradation. Understanding where and how natural connectivity is impaired is essential for managing, protecting and remediating these ecosystems. Wetland Interferometric Synthetic Aperture Radar (Wetland InSAR) can provide information on surface flow orientation in wetlands at a high spatial resolution, which can be used for the detection of hydrological barriers in the wetland. However, the broad application of this approach is constrained by the labour-intensive manual delineation of barriers based on mapped water levels. This study presents the first deep learning-based methodology for the automated detection of hydrological barriers. We trained a deep convolutional network to segment edge features of hydrological barriers in 22 image pairs captured by ALOS PALSAR-1 L-Band InSAR between 2006 and 2011. The training dataset consisted of manually labelled and delineated barriers showing abrupt changes in water surface elevation and wrapped interferograms with high coherence. The model was trained and tested on six wetland sites of varying fragmentation levels and wetland types in the United States, Cuba, Mexico, Colombia and Venezuela. Across these sites, the convolutional network detected hydrological barriers with up to 80% accuracy. The model performed particularly well in detecting linear hydrological barriers such as roads, levees and channels. Notably, we found that some barriers impede flow only seasonally, appearing during low water levels and disappearing when water levels rise. However, the model shows limitations in detecting barriers in highly dynamic environments with lower coherence. Our automated approach to detecting and assessing wetland hydrologic connectivity can be applied more broadly to support the effective management of fragmented wetland ecosystems.

1. Introduction

Hydrological connectivity controls the chemical composition, water availability and ecological structure of wetland ecosystems (Manzoni et al., 2020; Jaramillo et al., 2018). Connectivty describes the unimpeded flow of water influenced by tidal cycles, gravity and freshwater inflows or outflows (Ameli and Creed, 2017; Dai et al., 2020). It regulates several processes essential for ecosystem functioning and integrity (Pringle, 2003), including the propagation of plant seeds and propagules (Wang et al., 2019), the dispersal of fish and amphibians across their various life stages (Stoffels et al., 2022) as well as the transport of water, sediments and nutrients. However, landscape features like levees, channels or roads can obstruct surface hydrological connectivity within wetlands. As such, monitoring hydrological connectivity and the identification of barriers are critical for targeted conservation and restoration (Hermoso et al., 2012; Jaramillo et al., 2018; Jimenez and Lugo, 1985).

Numerous methods have been used to assess hydrological connectivity and fragmentation in wetlands. These include hydrological and hydrodynamic modelling (Ameli and Creed, 2017; Robinson et al., 2015), dye-tracing experiments (Dai et al., 2020) and various geospatial and optical remote sensing-based techniques (e.g. Li et al., 2021; Long

* Corresponding author at: Department of Physical Geography and Bolin Centre for Climate Research, Stockholm University, Stockholm SE-106 91, Sweden.
E-mail address: clara.hubinger@natgeo.su.se (C. Hübinger).

https://doi.org/10.1016/j.rse.2024.114314
Received 5 December 2023; Received in revised form 3 July 2024; Accepted 6 July 2024
Available online 16 July 2024
0034-4257/

and Pavelsky, 2013; Singh and Sinha, 2019; Vanderhoof et al., 2016; Wu and Lane, 2017; Zhao et al., 2009). The presence of barriers is directly linked to losses in surface hydrological connectivity in terms of continuous water surface height, slope or flow (Delgado et al., 2013; Huff and Feagin, 2017; Jaramillo et al., 2018; Liu et al., 2020; Tan et al., 2023). However, pinpointing the location of these barriers remains challenging, as their effects are often only measured and detected further downstream (Pringle, 2003).

The mapping of surface water extent with remote sensing complements traditional in-situ measurements of water depth and flow as it provides spatially continuous data at fine resolutions (Long and Pavelsky, 2013; Wu and Lane, 2017). In vegetated wetlands, however, the use of optical sensors is often limited by dense herbaceous vegetation or tree canopy. Due to its ability to penetrate clouds and emergent vegetation, Synthetic Aperture Radar (SAR) data has been used widely to monitor wetlans. In particular, SAR sensors with high wavelengths such as L-Band are useful for monitoring densely vegetated ecosystems such as wooded swamps and mangrove forests (Chapman et al., 2015; Rosenqvist et al., 2007).

Interferometric SAR (InSAR) over wetlands further leverages SAR

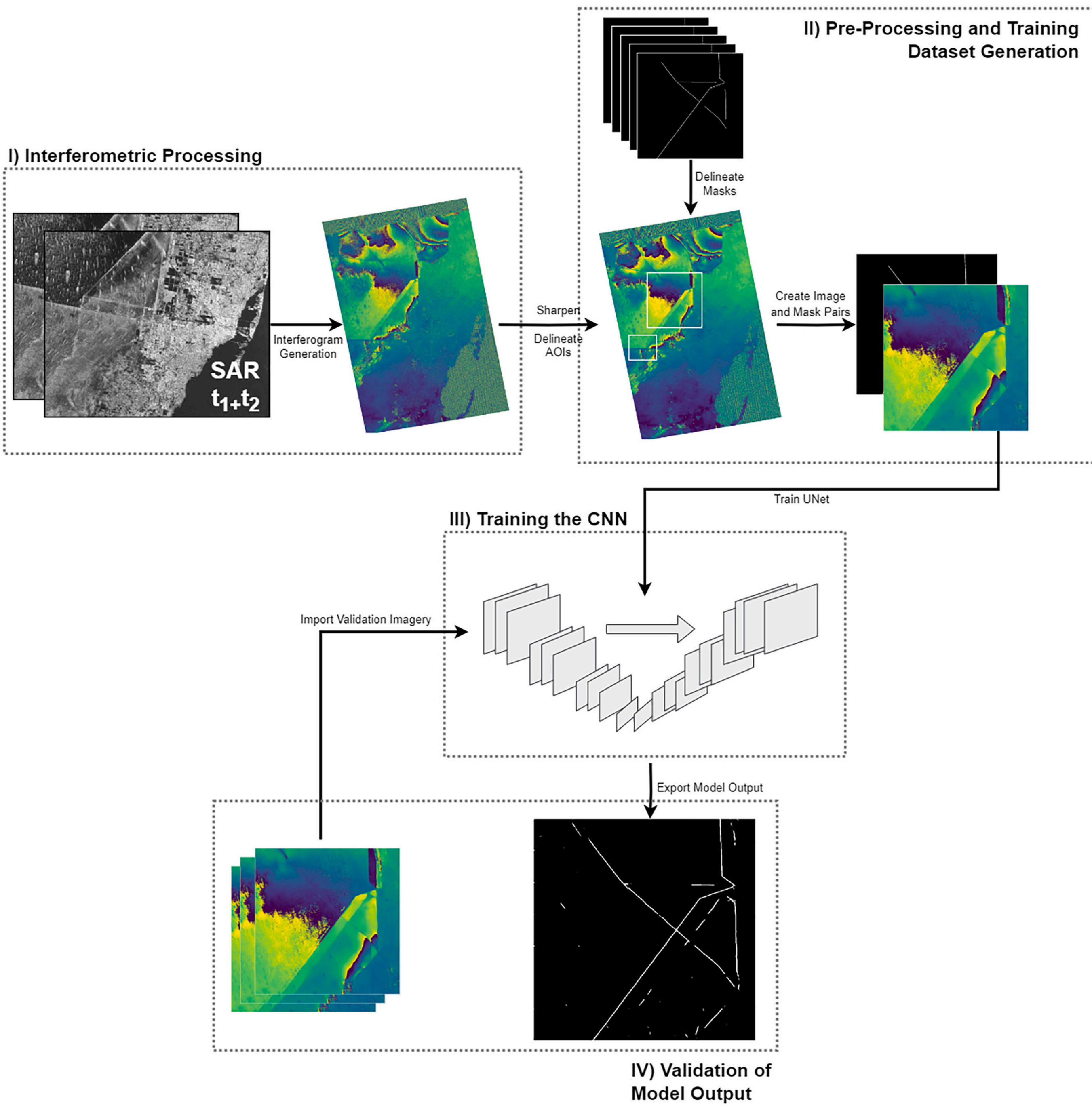

Fig. 1. Processing pipeline for classifying line features and detecting hydrological barriers in interferometric imagery over wetlands. The processing is performed in four steps: I) Several interferograms with short temporal baselines are created using ALOS-PALSAR 1 imagery over several wetlands with distinct fragmentation patterns, II) A training dataset is created using manually delineated reference masks to match discontinuous phase patterns in the interferometric imagery, III) The training dataset is fed into a UNet to automate the detection of the line features, IV) The performance of the segmentation model is assessed using precision, recall, F1 score and overall accuracy.

imagery by comparing pairs of images taken at the same orbital location at two different times to estimate water level change during the intervening period (Mohammadimanesh et al., 2018a). Wetland InSAR has been used for the assessment of water level changes in lakes (Palomino-Ángel et al., 2022; Aminjafari et al., 2024) and wetlands (Hong et al., 2010; Kim et al., 2009; Liao et al., 2020; Wdowinski et al., 2008; Xie et al., 2013), the monitoring of flood inundation extent (Canisius et al., 2019; Gondwe et al., 2010; Kim et al., 2017; Oliver-Cabrera and Wdowinski, 2016; Palomino-Ángel et al., 2019) and the classification of wetland types (Brisco et al., 2017; Chen et al., 2020). The technique relies on the signal from the double-bounce of inundated or emergent vegetation, meaning that significant changes in vegetation cover or transition to open water over time can induce a loss of coherence between InSAR signals (Oliver-Cabrera et al., 2022). By leveraging discontinuities in interferometric imagery over time across diverse wetland environments, InSAR has proven to be a powerful tool for identifying wetland hydrological barriers (Jaramillo et al., 2018; Liu et al., 2020).

While detecting hydrological barriers from InSAR is promising (e.g., Liu et al., 2020), manual delineation of barriers is burdensome and a task well suited for deep learning and computer vision automation. Supervised deep learning models have been used widely within remote sensing applications to identify features in optical and radar imagery (Ghamisi et al., 2016; Hu et al., 2015; Zhu et al., 2017). In wetlands, for example, optical (Liu et al., 2018; Rezaee et al., 2018) and multi-sensor approaches have been used for the classification of wetland types (Hosseiny et al., 2022; Mahdianpari et al., 2018) and the monitoring of inundation extent (Peña et al., 2024). As the phase differences from obstructions result in sharp discontinuities on either side of a hydrological barrier, InSAR data captured over wetlands is a good candidate for detecting hydrological barriers using similar image segmentation techniques.

Here, we propose the automated extraction of hydrological barriers from the segmentation of unwrapped phase interferograms, building on the InSAR methodology of Jaramillo et al. (2018) and Liu et al. (2020). We train and apply our automated method in six tropical wetlands to assess the ability of our segmentation approach to detect hydrological obstruction across a range of environments. Our model validation demonstrates it can identify barriers and evaluate their seasonal presence to help quantitatively assess hydrological connectivity in these sites.

2. Methodology

The methodology for classifying the hydrological obstructions in InSAR imagery is divided into four parts (Fig. 1). First, a reference dataset of barriers is manually generated by visual interpretation of interferometric imagery from several areas of interest and combined with manually delineated reference barrier masks (I and II). Next, the presence of line features within the InSAR imagery is predicted using a UNet-based supervised segmentation model (III) and the accuracy of the model output is evaluated through an independent validation (IV). Finally, the model output and reference dataset are analyzed using optical data and hydrological regime information to assess barrier presence over time and identify the types of barriers detected.

2.1. Study sites

We train and validate our barrier detection methodology over six tropical wetlands (Fig. 2A), where L-band InSAR proves useful due to its ability to penetrate dense vegetation with the SAR signal. To ensure an unbiased evaluation of the model performance and to avoid data leakage, the training dataset does not include Areas of Interest (AOIs) present in the validation dataset. Included in the training dataset are the western and northern parts of the Everglades, the Louisiana wetlands in the United States, and the Cienaga de Zapata in Cuba (Fig. 2). The validation dataset includes the eastern side of the Everglades, the Pantanos de Centla in Mexico, the northern Atrato River Floodplain in Colombia, and the Cienagas de Juan Manuel in Venezuela. Since large parts of the selected wetlands do not contain observable barriers, we concentrate on smaller AOIs with distinct barrier patterns for the training dataset (Fig. 2) while including larger areas for the validation AOIs (VAOIs) to assess the model's robustness across various wetland types on a broader scale.

In the Everglades, AOI 1 is located within the Big Cypress Preserve, a swamp area dominated by bald cypress trees (Welch, 1999), while AOIs 2–3 and VAOI 1 are situated in sawgrass marshes where water flow is regulated by multiple water conservation areas (Hong and Wdowinski, 2014). The area experiences a wet season during the summer months and dry weather during the winter. While the cypress and mangrove forests remain wet year-round, the drier weather during the winter results in the drying of the edges around the sawgrass marshes and the appearance of hammocks covered by grass along non-flooded land (Ordoyne and Friedl, 2008).

All AOIs in the Louisiana wetlands are located in the vegetated freshwater swamps surrounding the Mississippi River and Lake Maurepas. The wetlands in the area are highly fragmented, with roads and several flood control levees located along the Mississippi River (Oliver-Cabrera and Wdowinski, 2016). The AOI selected for the Ciénaga de Zapata includes a major channel along coastal marshes. Unlike the Everglades and the Louisiana wetland, the Ciénaga de Zapata does not have water control schemes.

The Pantanos de Centla is a wooded swamp wetland in the south of Mexico. Though it has been a protected Biosphere Reserve since 2006, there are several canals and roads present in the core area of the wetland in VAOI 2 (Guerra-Martínez and Ochoa-Gaona, 2008). Wetland marshes and forests cover the VAOI 3 selected along the northern edge of the Atrato floodplain. The area is one of the rainiest regions globally and faces encroachment by anthropogenic activity (Palomino-Ángel et al., 2019). Still, the selected region is of difficult access and rather pristine, only exhibiting few obstructions to water flow. Similarly, only a small number of barriers are observed in the swamp wetlands of the Cienagas de Juan Manuel, primarily located along the northern and southern edges of the wetland border in VAOI 4.

2.2. Interferometric processing

Active sensors such as SAR emit a radar beam and receive a reflected signal, providing information on backscattering intensity, phase (θ), and polarization influenced by ground surface properties. The signal phase represents the distance traveled by the radar signal before it reaches the ground surface and is presented as a number between $-\pi$ and π. An elevation change of the ground surface results in a different phase value in the returned radar signal. In a process called unwrapping, typical of InSAR, phase ambiguity larger than 2π phase cycles is removed to flatten the interferogram and make the remaining phase variation directly related to changes in surface height. Hence, the unwrapped phase difference between a reference and secondary signal recorded over a wetland can determine water level changes between the times the two signals were acquired. Apart from providing information on water level changes (i.e., direction and the rate of change), the fringe patterns visually representing the wrapped phase signal can vary in density, which can help distinguish between steep gradients in the water surface representing rapid flow from shallower gradients illustrative of slower flow. A pattern of abrupt phase change between adjacent pixels in the interferogram can identify the location of hydrological barriers. Such patterns have been observed in InSAR imagery in the Louisiana wetlands (Oliver-Cabrera and Wdowinski, 2016), the Everglades (Hong et al., 2010), the Ciénaga de Santa Marta (Jaramillo et al., 2018), and the Baiyangdian wetland (Liu et al., 2020).

This study employs ALOS-PALSAR 1 imagery, captured between 2006 and 2011 at L-Band wavelength in both single (FBS) and dual polarization (FBD) modes. L-Band data was chosen as it has been shown

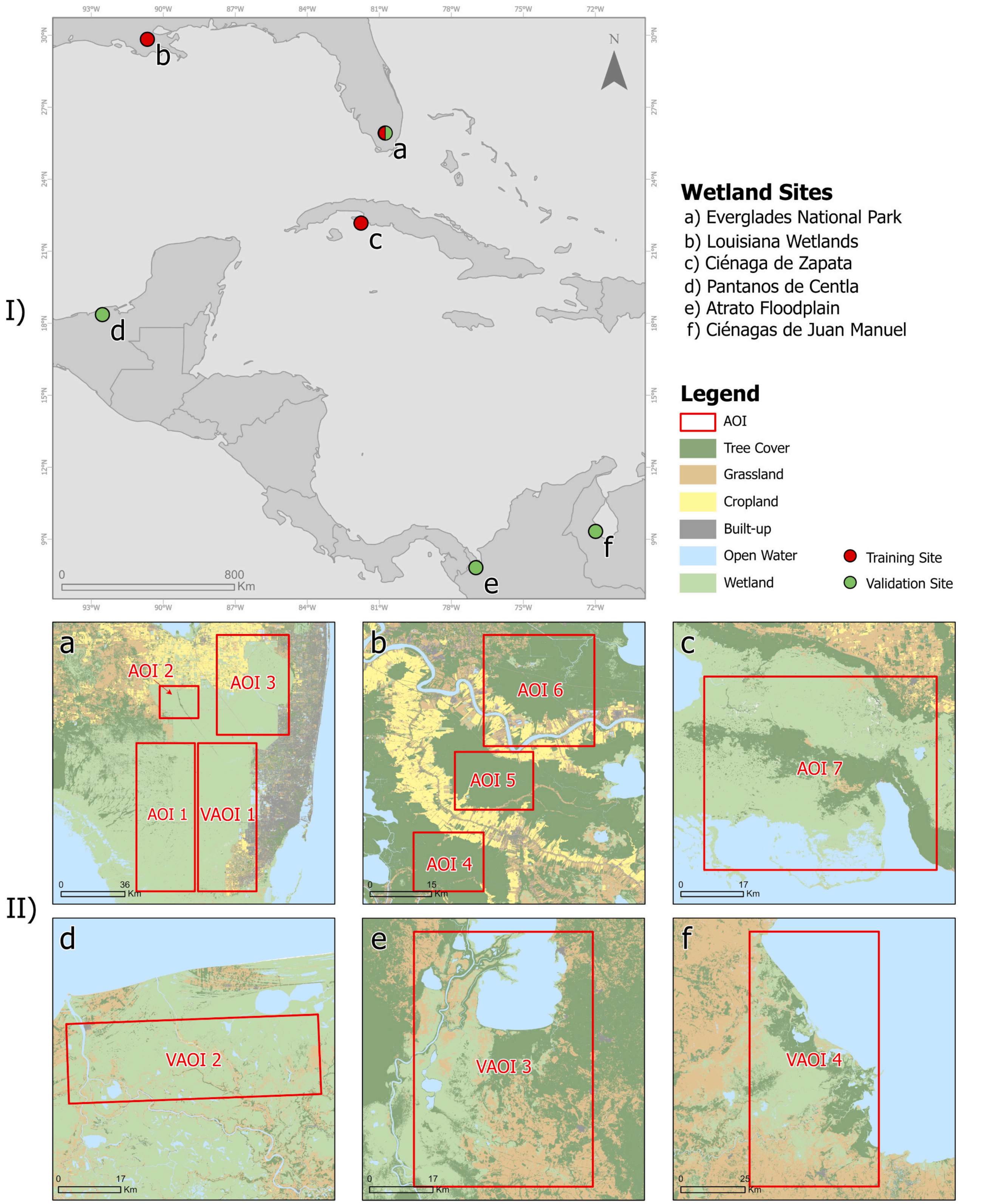

Fig. 2. Study Area and Areas of Interest (AOI) selected to create the training and validation dataset. 2 A) shows the location of the six wetlands, 2B) the land cover and location of the AOIs and validation AOIs (VAOIs) in each wetland. Imagery for the training dataset is collected over the Everglades (a), the Louisiana wetlands in the United States (b), and the Cienaga de Zapata in Cuba (c). The interferograms were clipped to the boundaries of AOIs, as shown in red, to include only data with distinct barrier patterns. We selected three AOIs in the Everglades, three in the Louisiana wetlands and one in the Cienaga de Zapata. The data for model validation was collected across four wetland over larger VAOIs in the Everglades, the Pantanos de Centla in Mexico (d), the Atrato River Floodplain in Colombia (e) and the Cienagas de Juan Manuel in Venezuela (f). The validation sites present varying degrees of fragmentation and land-use patterns, ranging from highly fragmented areas like the Everglades and Pantanos de Centla to less affected landscapes such as the Atrato Floodplain and the Cienagas de Juan Manuel. Land Cover Data retrieved from Dynamic World. (For interpretation of the references to colour in this figure legend, the reader is referred to the web version of this article.)

to retain a high correlation between the reference and secondary image in vegetated wetlands, even for longer temporal baselines, improving the quality of the InSAR image (Kim et al., 2013). All images were retrieved from the Alaskan Satellite Facility web portal. The images used for model training and validation are listed in Tables S1 and S2, respectively, in the supplementary material. The interferograms were generated by pairing images with the same flight path, frame, and the smallest temporal baseline. A 3-arc-second SRTM Digital Elevation Model (DEM) was utilized to remove the phase distortion caused by surface topography (the topographic phase) and geocode the final image. No atmospheric correction was applied to the imagery. All processing was done using the InSAR Scientific Computing Environment (ISCE). In total, 38 interferograms were generated across all wetland sites for the final training and validation datasets. Satellite revisit times for the image pairs ranged from 46 days to up to 277 days between reference and secondary image. Here, the interferograms were analyzed in the wrapped phase to retain the raw phase information and to avoid noise arising from unwrapping in areas with many discontinuities (Oliver-Cabrera et al., 2022).

2.3. Training and validation data of obstruction presence

A reference set of hydrological obstructions was manually delineated from a visual assessment of the interferograms (See selected image pairs for training and validation in supplementary material). We classified as barriers instances where we observe phase discontinuity in the InSAR image. This discontinuity is caused by different changes in water levels on either side of the barrier, indicating that these two parts of the wetland are subject to different hydrological changes. To facilitate interpretation, the interferogram speckle was smoothed using a median filter with a 3-pixel kernel size, and each smoothed wrapped phase was exported as a grayscale image with the values from - π to π and normalized between 0 and 255. Obstructions were delineated as line features in ArcGIS and then converted to polygons using 50-m buffers on each side of the barrier lines. Across the six case study sites, more than 690 distinct obstructions were delineated manually (see Table 1), amounting to a cumulative length of more than 2100 km. For both the training and validation datasets, we excluded scenes that did not show visible barrier patterns, including low-quality images where noise due to low coherence obscured distinct phase discontinuities, preventing the manual delineation of barriers, and images lacking visible barriers (a table with information on excluded scenes can be found in the supplementary material (Table S7), along with figures showing model predictions on excluded scenes (Fig. S2)). After the initial visual recognition, the digitized objects were manually filtered to retain only instances of true phase discontinuities. Fig. 3 shows an example of a phase discontinuity in the training dataset along line A-C (different colors on both sides of the line), representing a hydrological barrier (Fig. 3B) and a continuous phase not considered a hydrological barrier and hence discarded from the training dataset (Fig. 3C, line A-B; similar colors on both sides of the line). The final polygons were then converted to raster layers to match the grayscale interferograms. Before their use as input to the segmentation model, each pair of reference image and interferogram was split into tiles of 128×128 pixels in size. Finally, the size of the training dataset was increased through several data augmentation steps, including stretching, zooming into parts of the imagery, and reversing the phase values between - π and π. The final reference dataset consists of 1995 labelled tiles.

2.4. Implementation of the UNet

We employed a supervised segmentation model with a UNet structure to predict the linear features in the InSAR-wrapped phase interferogram. We selected a UNet structure because it has been successfully used to identify linear features in remotely sensed imagery and has shown good performance with training datasets of limited sizes (Hou et al., 2021; Yang et al., 2022). The UNet is set in a decoder-encoder architecture in which the spatial dimensions of the input data are first decreased through a combination of 3×3 convolutional and 2×2 MaxPooling layers to extract information about the image structure and then again increased through up-convolutional layers to create a segmentation mask (Ronneberger et al., 2015). The spatial information is retained between the decoder and encoder path through skipped connections at each convolutional layer. The model performs a binary classification on a per-pixel basis to determine the location of the line features in the input imagery.

We trained the network over 100 epochs with a batch size of 100 and a dropout rate of 0.06 over the entire training dataset consisting of 22 image pairs over 7 AOIs across 3 sites. The model weights were fitted to optimize a Binary Cross-entropy loss function (Ruby, 2020) as it provided higher overall accuracies than Dice loss (Dice, 1945) and Hinge loss functions (Wu and Liu, 2007). During model training, two metrics are used to assess overall model performance: the intersection over union (IOU) measuring the overlap between predicted and reference masks, and the loss measuring alignment between predictions and reference masks.

2.5. Model validation

Validation was performed on 16 scenes over four wetland sites (one VAOI per site) of different wetland types and fragmentation levels (sites shown in Fig. 2, scenes in supplementary material). Our approach involved a per-AOI out-of-sample validation due to the geographic partitioning of the training and validation sets, with only the Everglades sharing training and validation AOIs. The scenes were first georeferenced to align the reference and predicted barriers. Following suggested practices for the accuracy assessment of remote sensing based image classification, 1000 control points were distributed across the scenes using a random stratified sampling of barrier and non-barrier pixels (Olofsson et al., 2014). Only 800 control points were selected for each scene in the Atrato due to the limited number of barriers (the distribution of all ground control points are shown in Fig. S3 to S6 in the supplementary material). The resulting confusion matrices were used to calculate the performance scores precision, recall, F-score and overall map accuract (Everingham et al., 2015). The precision indicates the probability of a sample in the prediction correctly identifying a pixel in a line feature as follows:

$$Precision = \frac{True\ Positives}{(True\ Positives + False\ Positives)} \quad (1)$$

The true positives indicate when the model correctly identifies a pixel, while the false positives indicate pixels incorrectly identified as

Table 1
Summary of total area, number of scenes, and number of barriers (segments) delineated in the training and validation dataset across the wetland sites.

	Training Dataset				Validation Dataset		
	Area (km^2)	No. Scenes	No. Barriers		Area (km^2)	No. Scenes	No. Barriers
Everglades (West and North)	4860	9	201	Everglades (East)	2500	9	109
Louisiana	1070	10	245	Pantanos de Centla	1500	3	43
Zapata	3050	3	60	Atrato Floodplain	3220	2	11
				Cienagas de Juan Manuel	4900	2	25

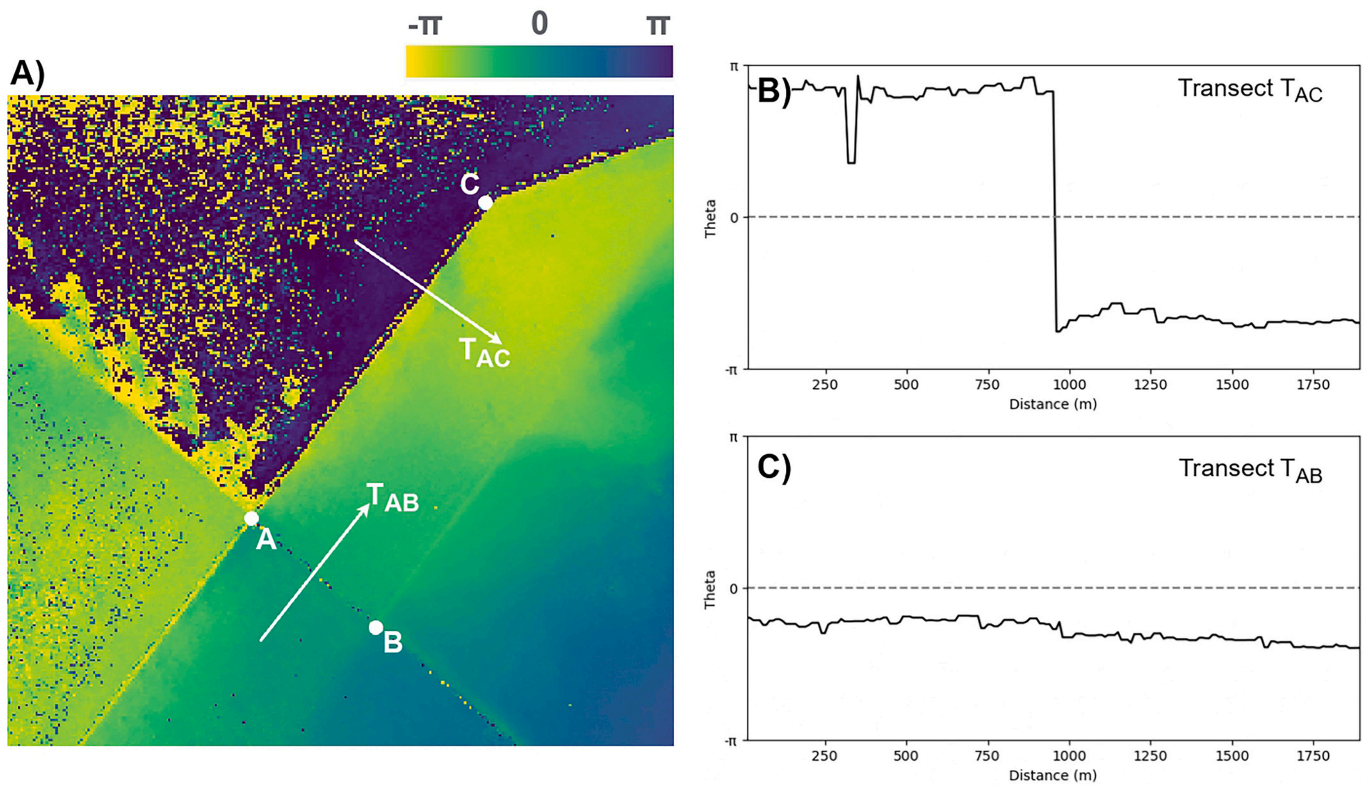

Fig. 3. A) Sample of an unwrapped interferogram over the Everglades from ALOS-1 images captured on 14 January 2008 and 29 February 2008. Transects T_{AB} and T_{AC} were considered for inclusion in the reference dataset. Candidate barriers of B) Phase value across transect T_{AC} C) Phase values across transect T_{AB}. As no distinct phase jump pattern can be seen in transect T_{AB}, it is excluded from the dataset, while T_{AC} is included.

edge features by the model. The recall score presents the number of positive samples correctly identified by the model as

$$Recall = \frac{True\ Positives}{(True\ Positives + False\ Negatives)} \quad (2)$$

where the false negatives are the number of pixels missed by the model in its prediction. The F1 score is calculated as the harmonic mean between precision and recall:

$$F1\ Score = 2 \times \frac{Precision \times Recall}{Precision + Recall} \quad (3)$$

The overall accuracy of each prediction map is calculated as:

$$Overall\ Accuracy = \frac{True\ Positives + True\ Negatives}{(Positives + Negatives)} \quad (4)$$

2.6. Temporal analysis of barrier presence in sample study site

We chose the Everglades as a sample study site to assess temporal dynamics in the presence of barriers and their relation to hydrological regimes. We calculated the barrier length in km for each scene in the validation dataset for VAOI1 (scenes pairs shown in table S1 in the supplementary material) and identified both permanent and conditional hydrological barriers (Liu et al., 2020) during dry and wet seasons. A permanent barrier is an area in the AOI showing a phase discontinuity in interferograms in both the dry and wet seasons, while a conditional barrier only shows a phase discontinuity in the dry season. The barriers can be either 1) man-made straight segments, signaling phase discontinuities in space due to a road, an embankment, or a drainage channel, or 2) not straight and following the occurrence of vegetation types or soil types on the landscape or the limit of a water body. In the case of 2, we assume these barriers to be naturally occurring.

3. Results

3.1. Model performance across wetland sites

The Fig. 4 shows two barrier maps spanning the entire Everglades, depicting the minimum cumulative barrier length at the end of the wet season (Fig. 2A) and the maximum at the end of the dry season (Fig. 2B). To capture the entire wetland, a composite image was created using three separate InSAR images along two flight paths (Fig. 2C). The fragmentation map was generated by combining barriers from the reference training dataset with model predictions from a validation dataset. In the black square, model predictions are presented, while the remaining barriers were manually delineated. The observed barrier length more than doubles from the wet season to the dry season, increasing from 114 km to 288 km, indicating increased fragmentation during the dry season. Notably, within VAOI1, the north-eastern side of the Everglades becomes almost entirely disconnected from the south-eastern side during this period.

During training, the model achieved a maximum IOU of 0.87 and a minimal loss of 0.01 on the dataset containing scenes from all wetland sites. When tested with the validation dataset, most performance metrics indicate that the model performs with similar accuracies across all wetland sites (see Table 2). Detailed confusion matrices for each site are provided in the supplementary material. These metrics demonstrate the robustness of the model across different wetland environments. Overall, the model attains an average precision of 0.99, a recall of 0.60, an F1 score of 0.74, and a final map accuracy of 80%. The Everglades, Pantanos de Centla, and the Cienagas de Juan Manuel achieve a similar recall score of 0.62 to 0.64, indicating that at least 35% of the barriers are not captured by the model. The lowest performance is observed in the Atrato Floodplains, where the recall score reveals that almost half of the barrier pixels are not correctly identified. However, the high precision scores achieved in all wetland sites suggest that although the model

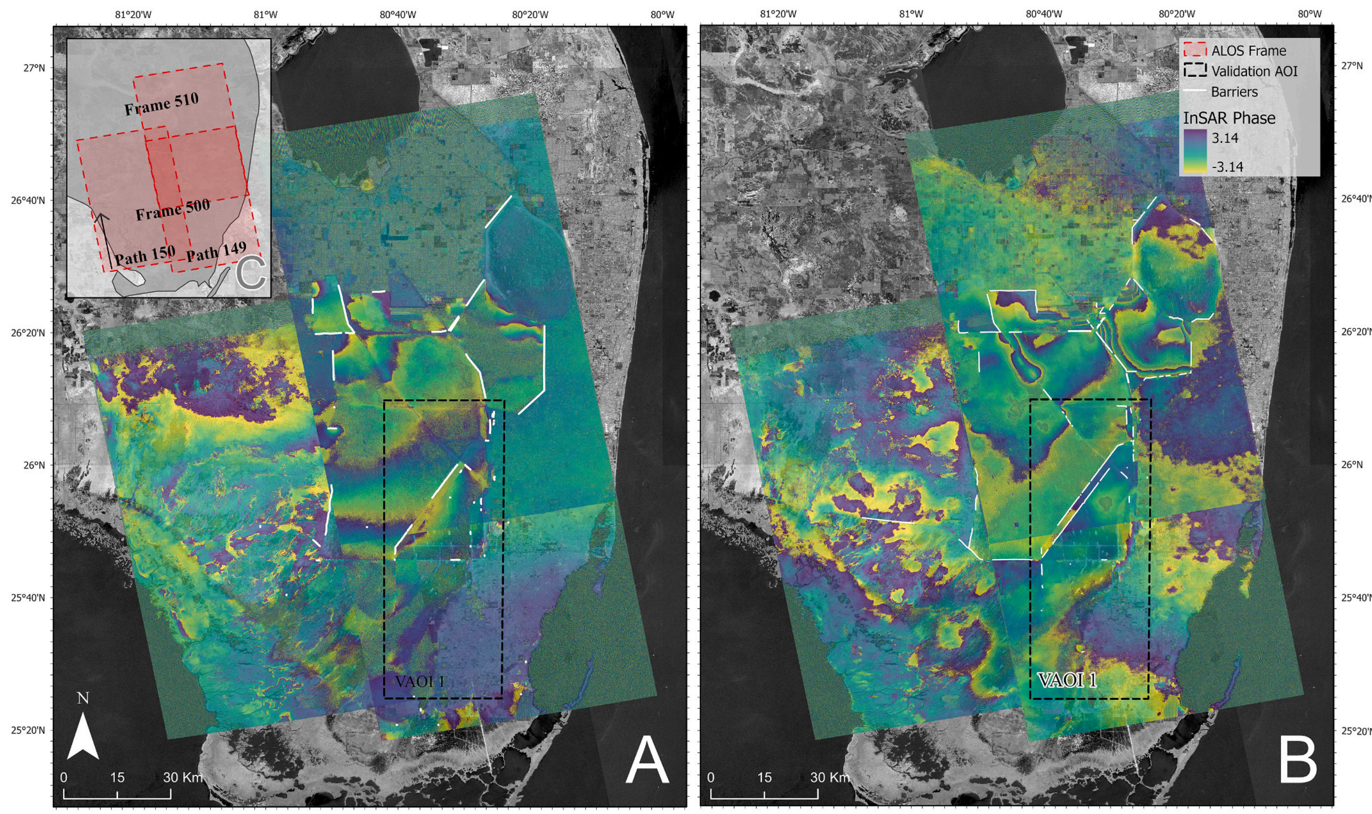

Fig. 4. Large scale barrier maps for a wet (Panel A; Path 149: October 19, 2009 - January 19, 2010, Path 150: December 21, 2009 - March 23, 2010) and dry (Panel B; Path 149: April 21, 2010 - June 6, 2010, Path 150: May 8, 2010 - June 23, 2010) period in the Everglades. Panel C shows the flight path and frame ID for the combined scenes used to produce the barrier map, the individual image frames are shown in red. Drawn in white is a composite of barriers from the reference and validation dataset. The black square shows the barriers predicted by themodel. Shown in the background is a mosaic of Alos-1 images for the year 2009 (provided by JAXA). (For interpretation of the references to colour in this figure legend, the reader is referred to the web version of this article.)

Table 2
Validation accuracy scores (precision, recall and F1 score) and number of scenes included across the four validation sites.

	Precision	Recall	F1 Score	Overall Accuracy	No. Scenes
Everglades	0.99	0.63	0.74	0.81	9
Pantanos de Centla	0.99	0.62	0.77	0.81	3
Atrato	1	0.54	0.70	0.77	2
Juan Manuel	1	0.62	0.76	0.81	2
Mean (across Scenes)	0.99	0.61	0.75	0.80	16

may underestimate barrier presence, its predictions are accurate.

To evaluate the strengths and weaknesses of the model, we visually inspect results over selected tiles across the study areas (Fig. 5). Accurate predictions are made in areas with high SAR signal coherence and hydrological barriers form distinct patterns of phase discontinuity.

In the Everglades, water levels change very gradually over a large area, resulting in a slow phase change across the landscape (seen in Fig. 4B in the VAOI 1). Barriers present in this wetland cut across extensive regions, entirely separating different parts. Fig. 5A illustrates an area with several barriers that divide surface water both vertically and horizontally. The different colors on either side of the fringe indicate that water levels have changed at different rates on the sides of these barrier. Due to the strong, distinct phase differences caused by the barriers, they are easily recognized by the model, as shown by the true positive prediction in Fig. 5B. However, when coherence is lowered, resulting in a speckled image, uncertainties are introduced (orange square in Fig. 5A).

In the Pantanos de Centla, open water in the form of small lakes and channels introduces low coherence patterns into the interferograms, complicating the prediction and identification of barriers. As a result, the less distinct appearance of barriers leads to false negative and positive predictions.(Fig. 5D). Similar patterns can be observed in the Cienagas de Juan Manuel, with two false negative predictions shown in Fig. 5E and F. In addition, the barriers in both these wetlands are not linear but may appear discontinuous and bent, further increasing the difficulty of detection by the model. This discontinuous barrier pattern and the surrounding phase values indicate that, unlike the barriers shown in the Everglades (Fig. 5A and B), they do not entirely separate parts of the wetland. Instead, they locally block surface water flow, causing the phase discontinuity seen in Fig. 5D. When the barrier ends and free water flow is restored, the phase gradually evens out, indicating that the water separation occurred only locally.

Finally, Fig. 5G shows a false positive prediction along an area of phase change caused by natural water level variations in the Atrato Floodplains. While the pattern displays a phase discontinuity, it is not due to a hydrological barrier but rather a phase cycle turnover from -π to π. This turnover occurs when the water level change exceeds the wavelength of the radar sensor. As the Atrato Floodplains are a very dynamic and rainy region, these phase turnover patterns are frequently observed. However, model prediction errors of this type remain minimal across the wetland sites.

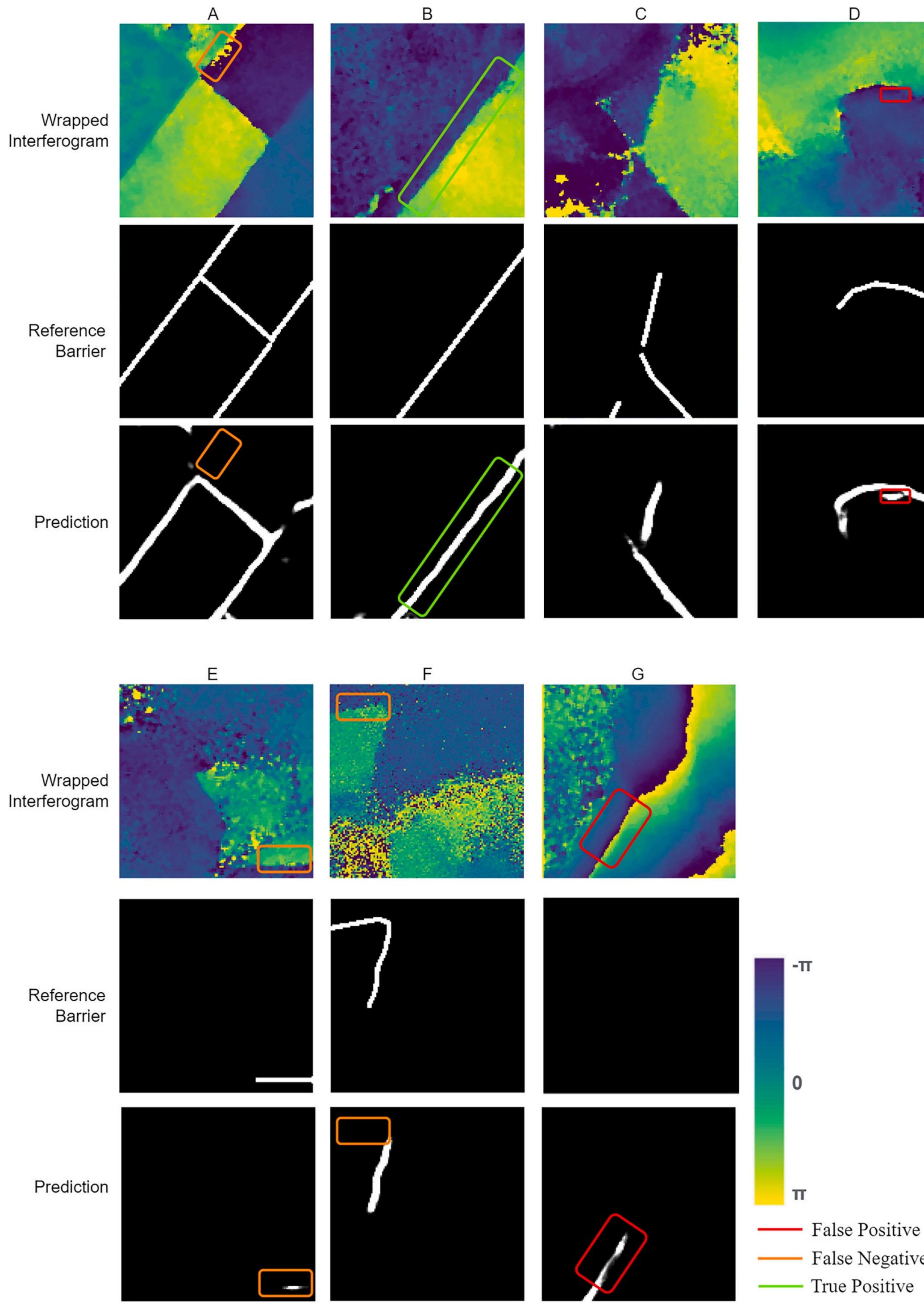

Fig. 5. Depiction of phase interferogram (row 1), reference barriers (row 2), and model prediction (row 3) across the Everglades (A-B), Pantanos de Centla (C-D), Cienaga de Juan Manuel (E-F) andthe Atrato Flood Basin (G); with the occurrence of true positive predictions of hydrological barriers (green), false negative predictions where the model misses part of a barrier (orange), and false positive predictions where the model detects a barrier where none is present in the reference mask (red). (For interpretation of the references to colour in this figure legend, the reader is referred to the web version of this article.)

3.2. Temporal analysis of hydrological barriers

Using the Everglades as our case study, we assessed the occurrence of hydrological barriers under varying hydrological conditions. To this end, we evaluated the barrier length from predicted scenes in the validation dataset into a time series of barrier permeability over multiple seasons (Fig. 6). The multitemporal analysis of the InSAR imagery over the Everglades shows that the length of detectable hydrological barriers varies across the dry and wet seasons.

Variations in water levels throughout the wet and dry seasons result in the formation of both permanent and conditional barriers within the wetland, with the conditional barriers obstructing water flow only during periods of low water levels. Seasons with high barrier presence are also associated with pools of water entirely isolated from the rest of the wetland, further fragmenting the wetland habitat. The total length of hydrological barriers in the Everglades AOI varies seasonally, with the

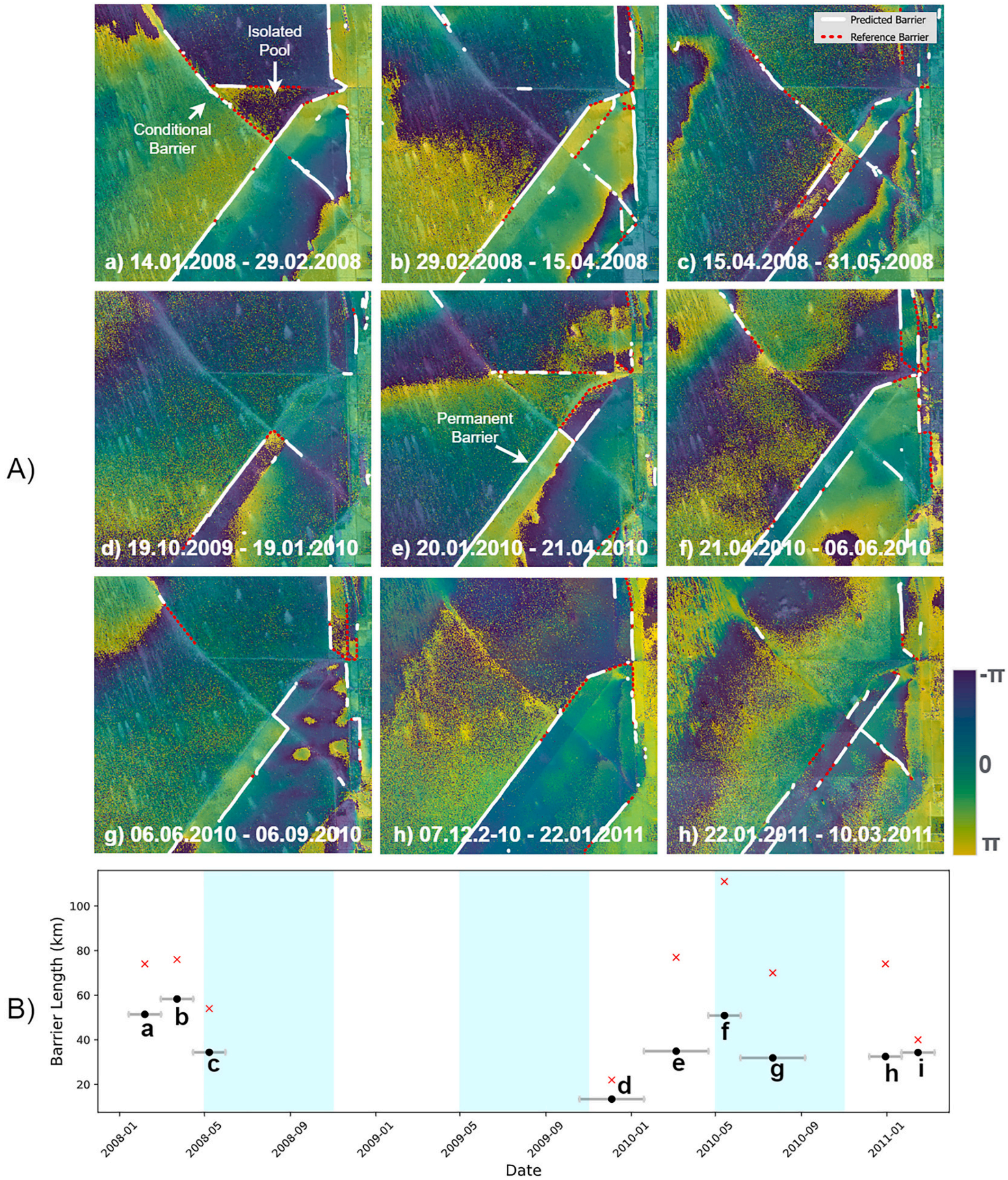

Fig. 6. Seasonal variations in the presence of hydrological barriers in AOI 1 in the Everglades across nine InSAR pairs based on model predictions. A) Interferograms captured over the Everglades with predicted barriers in white and missing reference barriers in dashed red, B) Total length of the predicted barriers in each interferogram during dry (October–April; white) and wet seasons (May to September; blue) shown in grey dots. The horizontal whiskers indicate the time between reference and secondary measurements. Length of the barriers in the reference dataset shown as red crosses. (For interpretation of the references to colour in this figure legend, the reader is referred to the web version of this article.)

wet season seeing a reduction in barrier length by more than half relative to the end of the dry season (Fig. 6, measurements c & d). Barrier length derived from images recorded during the dry season 2010 show increasing barrier length, with a peak at the beginning of the wet season.

3.3. Detection of different types of barriers

An inspection of our results and reference barriers can help us understand which types of barriers can be captured by the model. Using optical imagery alongside the interferogram confirms shows how channels (Fig. 7, column A) and roads (column B) can act as barriers. On the other hand, natural transitions, such as the change from mangrove to marsh vegetation in the Cienaga de Zapata (column C), also manifest as InSAR phase discontinuities and are identified as hydrological barriers by the model. As such, while the model demonstrates sensitivity to phase discontinuities, it is limited in discerning whether these arise from natural land-cover transitions or anthropogenic hydrological barriers.

The absence of a fringe discontinuity in column D suggests that despite the presence of a road in the optical image, surface water flow remains unobstructed. Similarly, column E shows an example of a barrier obstructing natural flow detected by InSAR but not seen in optical imagery due to dense vegetation in the Louisiana wetlands. This underscores the importance of using InSAR rather than optical methods to accurately identify instances of obstructed water flow.

4. Discussion

Our results show that deep learning models can be applied

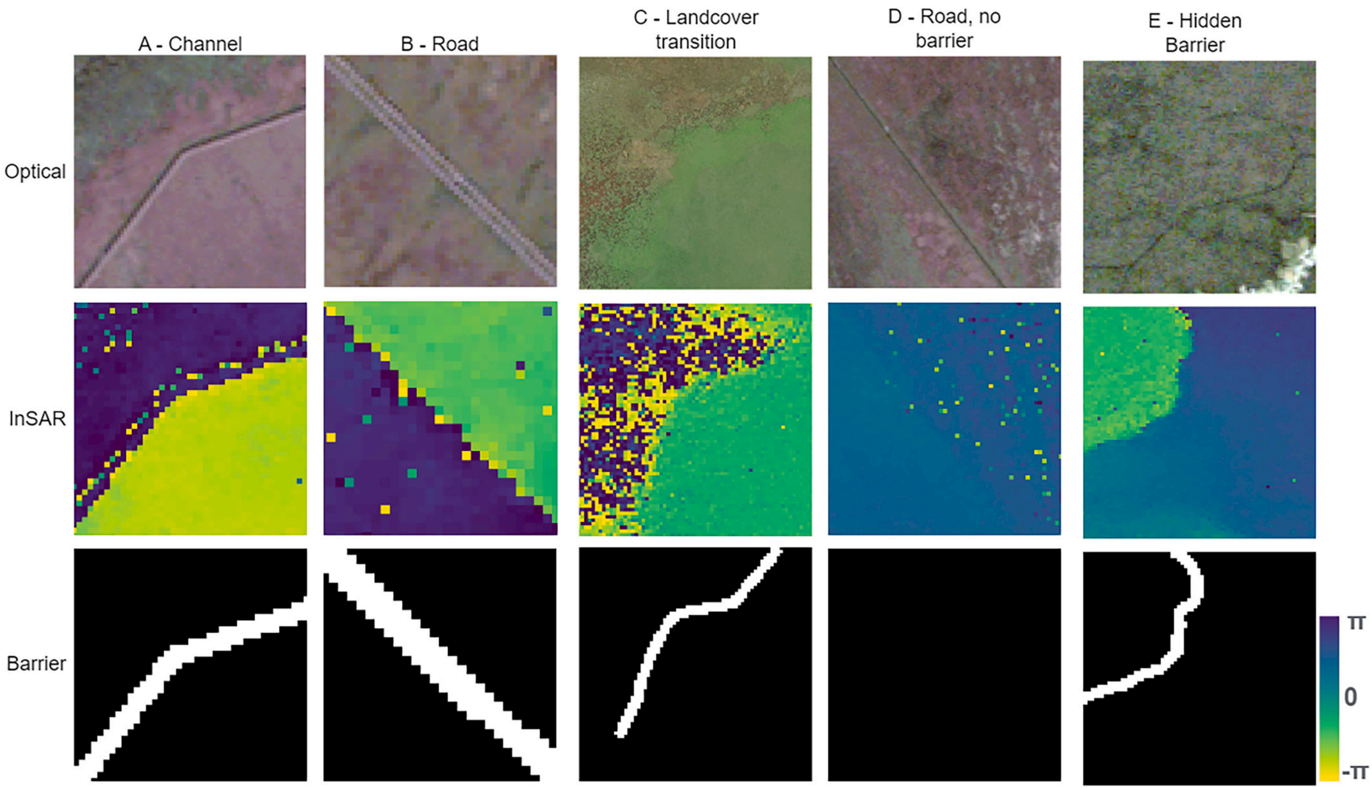

Fig. 7. Hydrological barriers observed in case study sites across the Everglades (A, B, and D), the Cienaga de Zapata (C) and the Louisiana wetlands (E). The barriers, depicted in white, were manually delineated based on phase discontinuities in InSAR imagery. Interferometric images were generated using Alos-1 data, with reference images recorded on January 14, 2008 (A, B and D), June 11, 2010 (C) and June 28, 2007 (E). Secondary images recorded on February 29, 2008 (A, B and D), July 27, 2010 (C) and September 28, 2007. Optical imagery was captured using Landsat-5 on October 3, 2009 (A, B and D) and September 20, 2007 (E), and Planet imagery for site C.

successfully for the automated mapping of hydrological barriers from interferometric imagery and a training set of manually labelled barriers. The methodology builds on previous InSAR-based techniques that detect hydrological barriers by identifying phase discontinuities in interferometric imagery. For instance, Jaramillo et al. (2018) identify several artificial channels acting as hydrological barriers using manual identification of these discontinuous patterns in Colombia's Cienaga Grande de Santa Marta. Expanding on this, Liu et al. (2020) identified barriers as disconnected fringes along transects. Here, we automate the detection of these phase discontinuities using a deep learning model trained with a manually labelled dataset of barriers.

Previous studies detecting hydrological barriers in wetlands utilized knowledge of local hydrological conditions and their changes over time to identify impediments to flow (Delgado et al., 2013; Huff and Feagin, 2017). Others employ hydraulic modelling techniques to quantify the impact of single barriers on hydrological connectivity (Tan et al., 2023), typically at a single wetland study site, as in Jaramillo et al. (2018) and Liu et al. (2020). Our automated methodology, however, can predict hydrological barriers across large areas of different regions and over time as long as high coherence can be retained in the InSAR images. This allows for the simultaneous monitoring of wetlands and the capture of seasonal patterns in the presence of hydrological barriers.

The predicted barriers from InSAR provide a rich data source for quantitative assessment and modelling of hydrology within wetlands. A broad-scale inventory of hydrological fragmentation is needed in many degraded inland and coastal wetlands worldwide and may be enabled by these InSAR measurements. Despite numerous studies of hydrological barriers in wetlands and river networks worldwide (Januchowski-Hartley et al., 2013; Belletti et al., 2020; Grill et al., 2019), the extent of lateral fragmentation within these environments and between floodplains and river systems is not fully documented (Knox et al., 2022; Steinfeld and Kingsford, 2013). Large-scale assessment of wetland disconnectivity is typically done through the encroachment of land uses in wetlands (Andreadis et al., 2022; Devitt et al., 2023; Fluet-Chouinard et al., 2023; Rajib et al., 2023) as well as databases of river levees (Ding et al., 2023) and coastal levees (Enwright et al., 2016). A fully automated approach utilizing InSAR could provide comprehensive estimates of hydrological fragmentation and seasonal permeability within wetland sites to assess the impairment associated with each barrier and target action to restore connectivity. By applying this method across entire wetlands and for multiple seasons, fragmentation indices could be developed for comparison across different sites and regions. In the future, with a longer record of InSAR pairs, this approach could also help evaluate the impact of climate oscillations and extreme events on wetland connectivity.

While the predictions of this first implementation of a barrier detection algorithm on interferometric imagery differ from the manual interpretation in some cases, the relatively small training set suggests a potential for development. The model performs best where coherence remains high between the two measurements, and tidal sheet flow results in continuous fringe patterns. As can be seen from both the performance scores and the application of the model in section 3.2, even though the precision is high, the model underestimates the presence of barriers by 37 to 46%. These errors are more prevalent in highly dynamic environments and areas with lower coherence around the barriers. As such, the model currently has a higher likelihood of performing well in more controlled environments, with the Everglades showing the lowest omission rates. As coherence depends on the time difference between the reference and secondary measurement, using radar images with shorter temporal baselines could enhance accuracies and increase the number of scenes that can be used by the model, since a considerable number of scenes are currently excluded due to noise (Canisius et al., 2019; Mohammadimanesh et al., 2018b). Lastly, it is worth noting that in this first implementation of the model, all instances where water flow is obstructed, resulting in a discontinuity of the fringe, are classified as barriers. Consequently, even natural shifts in wetland land cover may be identified as obstructions, though their impact on wetland health and fragmentation may differ from that of man-made barriers.

Increasing and diversifying the training dataset beyond the limited training data manually delineated from phase discontinuities in the InSAR images may improve model performance by addressing the current limitation of the omission of barriers. In future iterations of the model, automation of the training dataset generation may be implemented by incorporating augmented predictions from the model back into the training dataset or by adopting semi- and self-supervised strategies (Bountos et al., 2022). Similarly, employing a human-in-the-loop strategy, where a manual annotator performs a final augmentation step on the model predictions, can utilize existing computing resources while maintaining high classification accuracies (Cruz et al., 2021). Future research should explore adding further study sites for the generation of training data and incorporating additional SAR L-Band data from sensors such as ALOS-2 and SAOCOM (Satélite Argentino de Observación COn Microondas) to increase dataset sizes. Additionally, with a temporal baseline of 12 days and likely improved coherence between the measurements, the upcoming SAR L-band mission NISAR (NASA India Space Research Organization SAR) could be used in future iterations of this model for this purpose (Kellogg et al., 2020).

5. Conclusion

We present the first fully automated approach for the segmentation of barriers in wetlands by detection of phase discontinuities in InSAR imagery. Our Deep Neural Network model correctly identified barriers of different types; however, performance is affected in some cases by the coherence of the interferometric imagery.The ability of InSAR data to detect discontinuity in surface water level allows us to differentiate which static infrastructure, like roads and channels, acts as hydrological barriers to the water flow in wetlands and for how long. Furthermore, the model's ability to detect barriers hidden by vegetation underscores the significance of interferometric imagery over other methods for monitoring connectivity in wetlands. A high omission rate remains a limitation of the model, especially in highly dynamic environments with lower coherence. The capacity of the deep learning model to predict barriers across multiple wetland sites makes this methodology well suited for monitoring hydrological connectivity of wetlands sites globally to inform conservation and restoration efforts worldwide.

Funding

This project was funded by the Swedish Research Council (VR) Project 2021-05774.

CRediT authorship contribution statement

Clara Hübinger: Writing – original draft, Supervision, Methodology, Investigation, Formal analysis, Data curation, Conceptualization. **Etienne Fluet-Chouinard:** Writing – review & editing, Methodology, Investigation, Data curation. **Gustaf Hugelius:** Writing – review & editing, Methodology, Investigation, Data curation. **Francisco J. Peña:** Writing – review & editing, Methodology. **Fernando Jaramillo:** Writing – review & editing, Supervision, Methodology, Investigation, Funding acquisition, Data curation.

Declaration of competing interest

The authors declare that they have no known competing financial interests or personal relationships that could have appeared to influence the work reported in this paper.

Data availability

Data will be made available on request.

Appendix A. Supplementary data

Supplementary data to this article can be found online at https://doi.org/10.1016/j.rse.2024.114314.

References

Ameli, A.A., Creed, I.F., 2017. Quantifying hydrologic connectivity of wetlands to surface water systems. Hydrol. Earth Syst. Sci. 21, 1791–1808. https://doi.org/10.5194/hess-21-1791-2017.

Aminjafari, S., Brown, I.A., Frappart, F., Papa, F., Blarel, F., Mayamey, F.V., Jaramillo, F., 2024. Distinctive patterns of water level change in Swedish lakes driven by climate and human regulation. Water Resour. Res. 60 https://doi.org/10.1029/2023WR036160 e2023WR036160.

Andreadis, K.M., Wing, O.E.J., Colven, E., Gleason, C.J., Bates, P.D., Brown, C.M., 2022. Urbanizing the floodplain: global changes of imperviousness in flood-prone areas. Environ. Res. Lett. 17, 104024 https://doi.org/10.1088/1748-9326/ac9197.

Belletti, B., Garcia De Leaniz, C., Jones, J., Bizzi, S., Börger, L., Segura, G., Castelletti, A., Van De Bund, W., Aarestrup, K., Barry, J., Belka, K., Berkhuysen, A., Birnie-Gauvin, K., Bussettini, M., Carolli, M., Consuegra, S., Dopico, E., Feierfeil, T., Fernández, S., Fernandez Garrido, P., Garcia-Vazquez, E., Garrido, S., Giannico, G., Gough, P., Jepsen, N., Jones, P.E., Kemp, P., Kerr, J., King, J., Łapińska, M., Lázaro, G., Lucas, M.C., Marcello, L., Martin, P., McGinnity, P., O'Hanley, J., Olivo Del Amo, R., Parasiewicz, P., Pusch, M., Rincon, G., Rodriguez, C., Royte, J., Schneider, C.T., Tummers, J.S., Vallesi, S., Vowles, A., Verspoor, E., Wanningen, H., Wantzen, K.M., Wildman, L., Zalewski, M., 2020. More than one million barriers fragment Europe's rivers. Nature 588, 436–441. https://doi.org/10.1038/s41586-020-3005-2.

Bountos, N.I., Papoutsis, I., Michail, D., Anantrasirichai, N., 2022. Self-supervised contrastive learning for volcanic unrest detection. IEEE Geosci. Remote Sens. Lett. 19, 1–5. https://doi.org/10.1109/LGRS.2021.3104506.

Brisco, B., Ahern, F., Murnaghan, K., White, L., Canisus, F., Lancaster, P., 2017. Seasonal change in wetland coherence as an aid to wetland monitoring. Remote Sens. 9, 158. https://doi.org/10.3390/rs9020158.

Canisius, F., Brisco, B., Murnaghan, K., Van Der Kooij, M., Keizer, E., 2019. SAR backscatter and InSAR coherence for monitoring wetland extent, flood pulse and vegetation: a study of the Amazon lowland. Remote Sens. 11, 720. https://doi.org/10.3390/rs11060720.

Chapman, B., McDonald, K., Shimada, M., Rosenqvist, A., Schroeder, R., Hess, L., 2015. Mapping regional inundation with Spaceborne L-band SAR. Remote Sens. 7, 5440–5470. https://doi.org/10.3390/rs70505440.

Chen, Y., Qiao, S., Zhang, G., Xu, Y.J., Chen, L., Wu, L., 2020. Investigating the potential use of Sentinel-1 data for monitoring wetland water level changes in China's Momoge National Nature Reserve. PeerJ 8, e8616. https://doi.org/10.7717/peerj.8616.

Cruz, L.D., Sierra-Franco, C., Silva-Calpa, G., Raposo, A., 2021. Enabling autonomous medical image data annotation: a human-in-the-loop reinforcement learning approach. In: Presented at the 16th Conference on Computer Science and Intelligence Systems, pp. 271–279. https://doi.org/10.15439/2021F86.

Dai, L., Zhang, Y., Liu, Y., Xie, L., Zhao, S., Zhang, Z., Xizhi, L., 2020. Assessing hydrological connectivity of wetlands by dye-tracing experiment. Ecol. Indic. 119, 106840 https://doi.org/10.1016/j.ecolind.2020.106840.

Delgado, P., Hensel, P.F., Swarth, C.W., Ceroni, M., Boumans, R., 2013. Sustainability of a tidal freshwater marsh exposed to a Long-term hydrologic barrier and sea level rise: a short-term and decadal analysis of elevation change dynamics. Estuar. Coasts 36, 585–594. https://doi.org/10.1007/s12237-013-9587-2.

Devitt, L., Neal, J., Coxon, G., Savage, J., Wagener, T., 2023. Flood hazard potential reveals global floodplain settlement patterns. Nat. Commun. 14, 2801. https://doi.org/10.1038/s41467-023-38297-9.

Dice, L.R., 1945. Measures of the amount of ecologic association between species. Ecology 26, 297–302. https://doi.org/10.2307/1932409.

Ding, M., Lin, P., Gao, S., Wang, J., Zeng, Z., Zheng, K., Zhou, X., Yamazaki, D., Gao, Y., Liu, Y., 2023. Reversal of the levee effect towards sustainable floodplain management, Nat. Sustain. https://doi.org/10.1038/s41893-023-01202-9.

Enwright, N.M., Griffith, K.T., Osland, M.J., 2016. Barriers to and opportunities for landward migration of coastal wetlands with sea-level rise. Front. Ecol. Environ. 14, 307–316. https://doi.org/10.1002/fee.1282.

Everingham, M., Eslami, S.M.A., Van Gool, L., Williams, C.K.I., Winn, J., Zisserman, A., 2015. The Pascal visual object classes challenge: a retrospective. Int. J. Comput. Vis. 111, 98–136. https://doi.org/10.1007/s11263-014-0733-5.

Fluet-Chouinard, E., Stocker, B.D., Zhang, Z., Malhotra, A., Melton, J.R., Poulter, B., Kaplan, J.O., Goldewijk, K.K., Siebert, S., Minayeva, T., Hugelius, G., Joosten, H., Barthelmes, A., Prigent, C., Aires, F., Hoyt, A.M., Davidson, N., Finlayson, C.M., Lehner, B., Jackson, R.B., McIntyre, P.B., 2023. Extensive global wetland loss over the past three centuries. Nature 614, 281–286. https://doi.org/10.1038/s41586-022-05572-6.

Ghamisi, P., Chen, Y., Zhu, X.X., 2016. A self-improving convolution neural network for the classification of hyperspectral data. IEEE Geosci. Remote Sens. Lett. 13, 1537–1541. https://doi.org/10.1109/LGRS.2016.2595108.

Gondwe, B.R.N., Hong, S.-H., Wdowinski, S., Bauer-Gottwein, P., 2010. Hydrologic dynamics of the ground-water-dependent Sian Ka'an wetlands, Mexico, derived from InSAR and SAR data. Wetlands 30, 1–13. https://doi.org/10.1007/s13157-009-0016-z.

Grill, G., Lehner, B., Thieme, M., Geenen, B., Tickner, D., Antonelli, F., Babu, S., Borrelli, P., Cheng, L., Crochetiere, H., Ehalt Macedo, H., Filgueiras, R., Goichot, M., Higgins, J., Hogan, Z., Lip, B., McClain, M.E., Meng, J., Mulligan, M., Nilsson, C., Olden, J.D., Opperman, J.J., Petry, P., Reidy Liermann, C., Sáenz, L., Salinas-Rodríguez, S., Schelle, P., Schmitt, R.J.P., Snider, J., Tan, F., Tockner, K., Valdujo, P. H., Van Soesbergen, A., Zarfl, C., 2019. Mapping the world's free-flowing rivers. Nature 569, 215–221. https://doi.org/10.1038/s41586-019-1111-9.

Guerra-Martínez, V., Ochoa-Gaona, S., 2008. Evaluación del programa de manejo de la Reserva de la Biosfera Pantanos de Centla en Tabasco, México. Universidad y Ciencia 24 (2), 135–146. Universidad Juárez Autónoma de Tabasco, Dirección de Investigación y Posgrado.

Hermoso, V., Kennard, M.J., Linke, S., 2012. Integrating multidirectional connectivity requirements in systematic conservation planning for freshwater systems. Divers. Distrib. 18, 448–458. https://doi.org/10.1111/j.1472-4642.2011.00879.x.

Hong, S.-H., Wdowinski, S., 2014. Multitemporal multitrack monitoring of wetland water levels in the Florida Everglades using ALOS PALSAR data with interferometric processing. IEEE Geosci. Remote Sens. Lett. 11, 1355–1359. https://doi.org/10.1109/LGRS.2013.2293492.

Hong, S.-H., Wdowinski, S., Kim, S.-W., Won, J.-S., 2010. Multi-temporal monitoring of wetland water levels in the Florida Everglades using interferometric synthetic aperture radar (InSAR). Remote Sens. Environ. 114, 2436–2447. https://doi.org/10.1016/j.rse.2010.05.019.

Hosseiny, B., Mahdianpari, M., Brisco, B., Mohammadimanesh, F., Salehi, B., 2022. WetNet: A Spatial–Temporal Ensemble Deep Learning Model for Wetland Classification Using Sentinel-1 and Sentinel-2. IEEE Trans. Geosci. Remote Sens. 60, 1–14. https://doi.org/10.1109/TGRS.2021.3113856.

Hou, Y., Liu, Z., Zhang, T., Li, Y., 2021. C-UNet: complement UNet for remote sensing road extraction. Sensors 21, 2153. https://doi.org/10.3390/s21062153.

Hu, W., Huang, Y., Wei, L., Zhang, F., Li, H., 2015. Deep convolutional neural networks for hyperspectral image classification. J. Sens. 2015, 1–12. https://doi.org/10.1155/2015/258619.

Huff, T.P., Feagin, R.A., 2017. Hydrological barrier as a cause of salt marsh loss. J. Coast. Res. 77, 88–96. https://doi.org/10.2112/SI77-009.1.

Januchowski-Hartley, S.R., McIntyre, P.B., Diebel, M., Doran, P.J., Infante, D.M., Joseph, C., Allan, J.D., 2013. Restoring aquatic ecosystem connectivity requires expanding inventories of both dams and road crossings. Front. Ecol. Environ. 11, 211–217. https://doi.org/10.1890/120168.

Jaramillo, F., Brown, I., Castellazzi, P., Espinosa, L., Guittard, A., Hong, S.-H., Rivera-Monroy, V.H., Wdowinski, S., 2018. Assessment of hydrologic connectivity in an ungauged wetland with InSAR observations. Environ. Res. Lett. 13, 024003 https://doi.org/10.1088/1748-9326/aa9d23.

Jimenez, J.A., Lugo, A.E., 1985. Tree mortality in mangrove forests. Biotropica 17, 177–185. https://doi.org/10.2307/2388214.

Kellogg, K., Hoffman, P., Standley, S., Shaffer, S., Rosen, P., Edelstein, W., Dunn, C., Baker, C., Barela, P., Shen, Y., Guerrero, A.M., Xaypraseuth, P., Sagi, V.R., Sreekantha, C.V., Harinath, N., Kumar, R., Bhan, R., Sarma, C.V.H.S., 2020. NASA-ISRO Synthetic Aperture Radar (NISAR) Mission. In: 2020 IEEE Aerospace Conference. Presented at the 2020 IEEE Aerospace Conference. IEEE, Big Sky, MT, USA, pp. 1–21. https://doi.org/10.1109/AERO47225.2020.9172638.

Kim, J.-W., Lu, Z., Lee, H., Shum, C.K., Swarzenski, C.M., Doyle, T.W., Baek, S.-H., 2009. Integrated analysis of PALSAR/Radarsat-1 InSAR and ENVISAT altimeter data for mapping of absolute water level changes in Louisiana wetlands. Remote Sens. Environ. 113, 2356–2365. https://doi.org/10.1016/j.rse.2009.06.014.

Kim, S.-W., Wdowinski, S., Amelung, F., Dixon, T.H., Won, J.-S., 2013. Interferometric coherence analysis of the Everglades wetlands, South Florida. IEEE Trans. Geosci. Remote Sens. 51 (12), 5210–5224. https://doi.org/10.1109/TGRS.2013.2252956.

Kim, J.-W., Lu, Z., Gutenberg, L., Zhu, Z., 2017. Characterizing hydrologic changes of the great dismal swamp using SAR/InSAR. Remote Sens. Environ. 198, 187–202. https://doi.org/10.1016/j.rse.2017.06.009.

Knox, R.L., Wohl, E.E., Morrison, R.R., 2022. Levees don't protect, they disconnect: a critical review of how artificial levees impact floodplain functions. Sci. Total Environ. 837, 155773 https://doi.org/10.1016/j.scitotenv.2022.155773.

Li, Z., Sun, W., Chen, H., Xue, B., Yu, J., Tian, Z., 2021. Interannual and seasonal variations of hydrological connectivity in a large shallow wetland of North China estimated from Landsat 8 images. Remote Sens. 13, 1214. https://doi.org/10.3390/rs13061214.

Liao, T.-H., Simard, M., Denbina, M., Lamb, M.P., 2020. Monitoring water level change and seasonal vegetation change in the coastal wetlands of Louisiana using L-band time-series. Remote Sens. 12, 2351. https://doi.org/10.3390/rs12152351.

Liu, T., Abd-Elrahman, A., Morton, J., Wilhelm, V.L., 2018. Comparing fully convolutional networks, random forest, support vector machine, and patch-based deep convolutional neural networks for object-based wetland mapping using images from small unmanned aircraft system. GIScience Remote Sens. 55, 243–264. https://doi.org/10.1080/15481603.2018.1426091.

Liu, D., Wang, X., Aminjafari, S., Yang, W., Cui, B., Yan, S., Zhang, Y., Zhu, J., Jaramillo, F., 2020. Using InSAR to identify hydrological connectivity and barriers in a highly fragmented wetland. Hydrol. Process. 34, 4417–4430. https://doi.org/10.1002/hyp.13899.

Long, C.M., Pavelsky, T.M., 2013. Remote sensing of suspended sediment concentration and hydrologic connectivity in a complex wetland environment. Remote Sens. Environ. 129, 197–209. https://doi.org/10.1016/j.rse.2012.10.019.

Mahdianpari, M., Salehi, B., Mohammadimanesh, F., Homayouni, S., Gill, E., 2018. The first wetland inventory map of Newfoundland at a spatial resolution of 10 m using Sentinel-1 and Sentinel-2 data on the Google earth engine cloud computing platform. Remote Sens. 11, 43. https://doi.org/10.3390/rs11010043.

Manzoni, S., Maneas, G., Scaini, A., Psiloglou, B.E., Destouni, G., Lyon, S.W., 2020. Understanding coastal wetland conditions and futures by closing their hydrologic balance: the case of the Gialova lagoon, Greece. Hydrol. Earth Syst. Sci. 24, 3557–3571. https://doi.org/10.5194/hess-24-3557-2020.

Mohammadimanesh, F., Salehi, B., Mahdianpari, M., Brisco, B., Motagh, M., 2018a. Wetland water level monitoring using interferometric synthetic aperture radar (InSAR): a review. Can. J. Remote. Sens. 44, 247–262. https://doi.org/10.1080/07038992.2018.1477680.

Mohammadimanesh, F., Salehi, B., Mahdianpari, M., Brisco, B., Motagh, M., 2018b. Multi-temporal, multi-frequency, and multi-polarization coherence and SAR backscatter analysis of wetlands. ISPRS J. Photogramm. Remote Sens. 142, 78–93. https://doi.org/10.1016/j.isprsjprs.2018.04.013.

Oliver-Cabrera, T., Wdowinski, S., 2016. InSAR-based mapping of tidal inundation extent and amplitude in Louisiana coastal wetlands. Remote Sens. 8, 393. https://doi.org/10.3390/rs8050393.

Oliver-Cabrera, T., Jones, C.E., Yunjun, Z., Simard, M., 2022. InSAR phase unwrapping error correction for rapid repeat measurements of water level change in wetlands. IEEE Trans. Geosci. Remote Sens. 60, 1–15. https://doi.org/10.1109/TGRS.2021.3108751.

Olofsson, P., Foody, G.M., Herold, M., Stehman, S.V., Woodcock, C.E., Wulder, M.A., 2014. Good practices for estimating area and assessing accuracy of land change. Remote Sens. Environ. 148, 42–57.

Ordoyne, C., Friedl, M.A., 2008. Using MODIS data to characterize seasonal inundation patterns in the Florida Everglades. Remote Sens. Environ. 112, 4107–4119. https://doi.org/10.1016/j.rse.2007.08.027.

Palomino-Ángel, S., Anaya-Acevedo, J.A., Simard, M., Liao, T.-H., Jaramillo, F., 2019. Analysis of floodplain dynamics in the Atrato River Colombia using SAR interferometry. Water 11, 875. https://doi.org/10.3390/w11050875.

Palomino-Ángel, S., Vázquez, R.F., Hampel, H., Anaya, J.A., Mosquera, P.V., Lyon, S.W., Jaramillo, F., 2022. Retrieval of simultaneous water-level changes in Small Lakes with InSAR. Geophys. Res. Lett. 49 https://doi.org/10.1029/2021GL095950 e2021GL095950.

Peña, F.J., Hübinger, C., Payberah, A.H., Jaramillo, F., 2024. DeepAqua: semantic segmentation of wetland water surfaces with SAR imagery using deep neural networks without manually annotated data. Int. J. Appl. Earth Obs. Geoinf. 126, 103624 https://doi.org/10.1016/j.jag.2023.103624.

Pringle, C., 2003. What is hydrologic connectivity and why is it ecologically important? Hydrol. Process. 17, 2685–2689. https://doi.org/10.1002/hyp.5145.

Rajib, A., Zheng, Q., Lane, C.R., Golden, H.E., Christensen, J.R., Isibor, I.I., Johnson, K., 2023. Human alterations of the global floodplains 1992–2019. Sci. Data 10, 499. https://doi.org/10.1038/s41597-023-02382-x.

Rezaee, M., Mahdianpari, M., Zhang, Y., Salehi, B., 2018. Deep convolutional neural network for complex wetland classification using optical remote sensing imagery. IEEE J. Sel. Top. Appl. Earth Obs. Remote Sens. 11, 3030–3039. https://doi.org/10.1109/JSTARS.2018.2846178.

Robinson, S.J., Souter, N.J., Bean, N.G., Ross, J.V., Thompson, R.M., Bjornsson, K.T., 2015. Statistical description of wetland hydrological connectivity to the river Murray in South Australia under both natural and regulated conditions. J. Hydrol. 531, 929–939. https://doi.org/10.1016/j.jhydrol.2015.10.006.

Ronneberger, O., Fischer, P., Brox, T., 2015. U-net: Convolutional networks for biomedical image segmentation. In: Navab, N., Hornegger, J., Wells, W.M., Frangi, A.F. (Eds.), Medical Image Computing and Computer-Assisted Intervention – MICCAI 2015, Lecture Notes in Computer Science. Springer International Publishing, Cham, pp. 234–241. https://doi.org/10.1007/978-3-319-24574-4_28.

Rosenqvist, A., Shimada, M., Ito, N., Watanabe, M., 2007. ALOS PALSAR: a pathfinder Mission for global-scale monitoring of the environment. IEEE Trans. Geosci. Remote Sens. 45, 3307–3316. https://doi.org/10.1109/TGRS.2007.901027.

Ruby, U., 2020. Binary cross entropy with deep learning technique for image classification. Int. J. Adv. Trends Comput. Sci. Eng. 9, 5393–5397. https://doi.org/10.30534/ijatcse/2020/175942020.

Singh, M., Sinha, R., 2019. Evaluating dynamic hydrological connectivity of a floodplain wetland in North Bihar, India using geostatistical methods. Sci. Total Environ. 651, 2473–2488. https://doi.org/10.1016/j.scitotenv.2018.10.139.

Steinfeld, C.M.M., Kingsford, R.T., 2013. Disconnecting the floodplain: Earthworks and their ecological effect in a dryland floodplain in the Murray–Darling Basin, Australia. River Res. Appl. 29, 206–218. https://doi.org/10.1002/rra.1583.

Stoffels, R.J., Humphries, P., Bond, N.R., Price, A.E., 2022. Fragmentation of lateral connectivity and fish population dynamics in large rivers. Fish Fish. 23, 680–696. https://doi.org/10.1111/faf.12641.

Tan, Z.Q., Yao, J., Gong, L.Q., Li, Y.L., Zhang, Q., Wang, X.L., Wan, R.R., Li, B., 2023. Multidirectional shifts in hydrological connectivity result from hydraulic barriers. Water Resour. Res. 59 https://doi.org/10.1029/2022WR033617 e2022WR033617.

Vanderhoof, M.K., Alexander, L.C., Todd, M.J., 2016. Temporal and spatial patterns of wetland extent influence variability of surface water connectivity in the prairie pothole region, United States. Landsc. Ecol. 31, 805–824. https://doi.org/10.1007/s10980-015-0290-5.

Wang, W., Li, X., Wang, M., 2019. Propagule dispersal determines mangrove zonation at intertidal and estuarine scales. Forests 10, 245. https://doi.org/10.3390/f10030245.

Wdowinski, S., Kim, S.-W., Amelung, F., Dixon, T.H., Miralles-Wilhelm, F., Sonenshein, R., 2008. Space-based detection of wetlands' surface water level changes from L-band SAR interferometry. Remote Sens. Environ. 112, 681–696. https://doi.org/10.1016/j.rse.2007.06.008.

Welch, R., 1999. Mapping the Everglades.
Wu, Q., Lane, C.R., 2017. Delineating wetland catchments and modeling hydrologic connectivity using lidar data and aerial imagery. Hydrol. Earth Syst. Sci. 21, 3579–3595. https://doi.org/10.5194/hess-21-3579-2017.
Wu, Y., Liu, Y., 2007. Robust truncated hinge loss support vector machines. J. Am. Stat. Assoc. 102, 974–983. https://doi.org/10.1198/016214507000000617.
Xie, C., Shao, Y., Xu, J., Wan, Z., Fang, L., 2013. Analysis of ALOS PALSAR InSAR data for mapping water level changes in Yellow River Delta wetlands. Int. J. Remote Sens. 34, 2047–2056. https://doi.org/10.1080/01431161.2012.731541.
Yang, M., Yuan, Y., Liu, G., 2022. SDUNet: road extraction via spatial enhanced and densely connected UNet. Pattern Recogn. 126, 108549 https://doi.org/10.1016/j.patcog.2022.108549.
Zhao, R., Chen, Y., Zhou, H., Li, Y., Qian, Y., Zhang, L., 2009. Assessment of wetland fragmentation in the Tarim River basin, western China. Environ. Geol. 57, 455–464. https://doi.org/10.1007/s00254-008-1316-y.
Zhu, X.X., Tuia, D., Mou, L., Xia, G.-S., Zhang, L., Xu, F., Fraundorfer, F., 2017. Deep learning in remote sensing: a comprehensive review and list of resources. IEEE Geosci. Remote Sens. Mag. 5, 8–36. https://doi.org/10.1109/MGRS.2017.2762307.